



**HAL**  
open science

## Capillary bulldozing of sedimented granular material confined in a millifluidic tube

Guillaume Dumazer, Bjørnar Sandnes, Knut Jørgen Måløy, Eirik G. Flekkøy

► **To cite this version:**

Guillaume Dumazer, Bjørnar Sandnes, Knut Jørgen Måløy, Eirik G. Flekkøy. Capillary bulldozing of sedimented granular material confined in a millifluidic tube. *Physical Review Fluids*, 2020, 5 (3), pp.034309. 10.1103/PhysRevFluids.5.034309 . emse-02543436

**HAL Id: emse-02543436**

**<https://hal-emse.ccsd.cnrs.fr/emse-02543436>**

Submitted on 11 Jun 2020

**HAL** is a multi-disciplinary open access archive for the deposit and dissemination of scientific research documents, whether they are published or not. The documents may come from teaching and research institutions in France or abroad, or from public or private research centers.

L'archive ouverte pluridisciplinaire **HAL**, est destinée au dépôt et à la diffusion de documents scientifiques de niveau recherche, publiés ou non, émanant des établissements d'enseignement et de recherche français ou étrangers, des laboratoires publics ou privés.

# Capillary bulldozing of sedimented granular material confined in a millifluidic tube.

Guillaume Dumazer,<sup>1,2</sup> Bjørnar Sandnes,<sup>3</sup> Knut Jørgen Måløy,<sup>1</sup> and Eirik G. Flekkøy<sup>1</sup>

<sup>1</sup>*PoreLab, The Njord center, University of Oslo, P.O. Box 1048 Blindern Oslo, Norway*

<sup>2</sup>*Mines Saint-Etienne, Univ Lyon, CNRS, UMR 5307 LGF, Centre SPIN, F-42023 Saint-Etienne France*

<sup>3</sup>*College of Engineering, Swansea University, Bay Campus, Swansea SA1 8EN, UK*

The motion of a capillary interface across a deformable granular material in a confined geometry shows the complex interplay between viscous forces, solid friction and capillary forces. In a horizontal quasi one-dimensional geometrical confinement, a millifluidic tube, the displacement of a three-phase flow consisting of two fluids and a mobile granular phase exhibits viscous or frictional displacement regimes, as shown in [*Phys. Rev. Lett.* **117**, 028002 (2016)]. In the present paper we explore in details the dynamics in both regimes by making use of a new set of data. The viscous displacement regime which is characterized by a fluidization of the immersed granular material dragged by the flow driving the displacement of the capillary interface is interpreted from a rheological point of view. The frictional displacement regime which displays a self-structuring of the granular material left in the tube behind the invading capillary interface, is interpreted with a model based on the Janssen's law able to predict the typical size of the plugs obtained.

## INTRODUCTION

Tube flows represent an idealized geometrical configuration to explain or predict the transport of fluid as a response to a pressure gradient. The flow rate  $Q$  resulting from an imposed pressure difference  $\Delta P$  along a duct of length  $L$  and cross-section  $\pi R^2$  is well established through the Hagen-Poiseuille equation relating the viscosity of the fluid  $\eta$  to the flow characteristics. This simple flow configuration exhibits interesting features if the flowing fluid is complex as with a multiphase flow [1], lava flow [2, 3] or blood transport [4–6].

This paper is investigating the displacement regimes of a gas/liquid interface along a millifluidic tube initially filled with a homogeneously sedimented granular material immersed in the liquid phase. As already reported in [1], the complex interplay between capillary forces, frictional and viscous dissipation is responsible for the development of several displacement regimes. The effect of the capillary forces in flow conditions dominated by viscous dissipation is the gradual fluidization of the entire granular material. On the other hand capillary forces in flow conditions dominated by frictional dissipation generate the self-structuring of the granular phase in regular plugs left in the wake of the moving interface. To develop further the observations reported in [1] we make use of a new set of data to understand and model the pressure evolution in each displacement regime.

The system investigated is featuring specific ingredients rarely studied together: (i) viscous dissipation, (ii) solid friction, and (iii) capillarity.

Flows of dense suspensions provide examples of systems where the combination of viscous dissipation and solid friction comes into play, and produce complex non-Newtonian rheological behaviours [7]. The effective viscosity of a suspension increases with the filling fraction of the solid particles [8, 9], with a singularity near the close packing fraction. The effective viscosity tends to infinity

when approaching the jamming transition [10]. Suspensions with large filling fractions exhibit also a non-linear evolution of the viscosity with the shear-rate, as illustrated by the discontinuous shear-thickening appearing as a sudden increase in effective viscosity [11, 12]. Another class of complex flows based on similar combination of dissipation mechanisms is provided by pneumatic and hydraulic conveying of granular materials. A rich variety of transport regimes can develop determined by the concentration in granular matter, and by the imposed carrying fluid flow rate [13–15].

If now we consider the effect of capillarity associated with various degrees of viscous dissipation in a porous media, several invasion patterns emerge [16, 17]. The capillary number measuring the viscous to capillary forces ratio is controlling the development of viscous fingering versus capillary fingering [18, 19].

The combination of viscous dissipation, solid friction and capillarity has been explored with pattern formation in so-called frictional fluids [20–22]. Here as well a rich variety of interface displacement pattern have been observed, ranging from viscous fingering [23, 24], to intermittent stick-slip dynamics forming frictional fingers [25, 26], or fracturing [27, 28]. The geometrical confinement used in these studies where a quasi two-dimensional Hele-Shaw cells. The parameters controlling the developing pattern are the initial filling fraction in granular matter, the compressibility of the system, the imposed flow rate, the effective gravity.

In this paper we explored in details the two main gas/liquid displacement regimes in a horizontal millifluidic tube partially filled with a granular phase, dominated either by viscous dissipation, or by solid friction. The gas/liquid interface is displaced by means of a syringe pump withdrawing the liquid initially filling the tube and saturating the sedimented granular phase. The regime dominated by viscous dissipation is studied from a rheological point of view to interpret the pressure evolution

during the tube evacuation. In the regime dominated by solid friction, the self-structuring of the granular matter into regular plugs formation is investigated for various initially filling fractions and bead diameters. A theoretical model is established, based on the Janssen stress law [30], which accounts for the perpendicular stress reorientation in a granular packing from a main load direction due to an underlying network of force chains [31]. A frictional length  $\lambda$  is derived from experimental measurements and is used to inform a predictive interpretation of the formed plug length. Eventually the cross-over from the viscous to frictional regime, already documented in our previous paper [1], is revisited with a generalized phase diagram based on dimensionless parameters.

## MATERIAL AND METHODS

### Experimental setup

We use a simple model of a confined three phase frictional flow. A horizontal millifluidic glass tube of length 1 m and internal diameter 2.0 mm is filled with a mixture of water and granular material. We choose a tube's diameter lower than the capillary length of water in air  $l_c \approx 2.4$  mm. If the tube's diameter were too large the air/liquid meniscus would collapse by gravity and a liquid film would spread along the bottom side of the tube. Using a small internal tube's diameter maintains the meniscus vertical on the tube's cross section. The internal surface of the glass tube is treated with a silanization solution (Fluka BioChemika 85126, [Dimethyldichlorosilane]) to achieve neutral wetting with approximately  $90^\circ$  contact angle. A meniscus perpendicular to the tube surface is more efficient at sweeping the grains along compared to a meniscus stretched out on a hydrophilic glass surface that tends to leave a residue of granular material sticking on the glass surface.

The tube is open to atmosphere on one end, and connected to a syringe pump on the other end as illustrated in Fig. 1(a). The syringe pump is used to drive the gas/liquid interface by selecting a desired volumetric flow-rate value  $I_0$ . We use a glass syringe with a limited amount of tubing in order to minimize the compressibility of the system. It has been shown in previous work that the compressibility of the system has a strong impact on the type of pattern observed in Hele-Shaw cells [22]. A flow-through pressure sensor (Honeywell Flow-through 26PCXXG6G) is placed at the tube's end connected to the syringe, in order to have access to the pressure difference  $\Delta P(t) = P_{atm} - P(t)$  along the tube.

We use glass beads sieved in different beads diameter ranges  $d_{beads} \in [53 - 75], [75 - 100], [100 - 150], [150 - 200], [200 - 300] \mu\text{m}$ . The density of the glass beads is measured at a value  $\rho_g \approx 2.5 \times 10^3 \text{ kg m}^{-3}$ .

The initial configuration of the system consists of a ho-

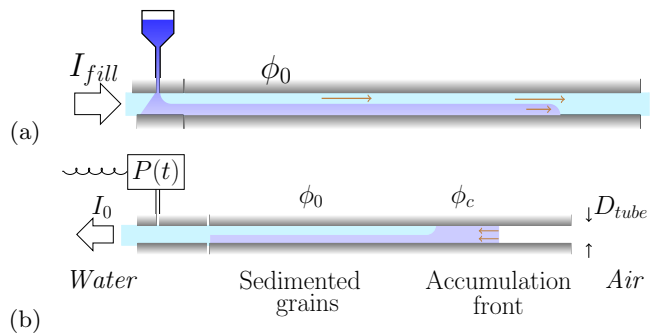


FIG. 1. (a) Schematics illustrating the filling procedure. A flow rate  $I_{fill}$  is imposed by the syringe pump in the tube. A closed hopper containing the glass beads and water is located above the tube's inlet. The sedimented glass beads dragged along the tube have a normalized filling fraction  $\phi_0$  corresponding to the fraction of the tube's cross-sectional area occupied by the sedimented granular material.

(b) Schematics of the experimental setup. A syringe pump withdraws water at constant rate  $I_0$  from the horizontal millifluidic tube. The mixture of grains and water initially sedimented is perturbed by the progress of the gas/liquid interface driven by the withdrawing rate. The pressure  $P(t)$  imposed by the pump is measured at the tube's outlet.

homogeneously sedimented layer of granular matter inside the horizontal tube. To prepare the system we produce a steady transport of granular matter along the tube, see on Fig. 1 (a). A steady flow of water only is first established in the tube by pumping in water at a flow rate  $I_{fill}$ . The granular matter is then poured inside the stream from a hopper located between the syringe pump and the tube, see figure 1 (a). The hopper is sealed and filled with water and glass beads. The granular matter falls freely from the hopper into the flow produced by the syringe pump and invades gradually the horizontal tube. The pump is stopped when the layer of sedimented granular material stretches the entire length of the tube. The filling fraction  $\phi_0$  obtained is a decreasing function of the imposed flow rate  $I_{fill}$ . We consider in this paper the initial filling fraction  $\phi_0$  in reduced units, as a fraction of the maximal filling fraction  $\varphi_c = 0.6$  corresponding to a loose random packing.

After preparing the initial state, with one end of the tube connected to the syringe and the second end open to the atmosphere, the fluid flow is reversed such that water is withdrawn from the glass tube. The gas/liquid meniscus at the open end of the tube starts to move into the tube interacting with the sedimented layer of glass beads. The invading meniscus perturbs the sedimented layer of granular material. The physical processes we are investigating take place during this displacement of the meniscus. Once the meniscus has traveled along the whole tube, the experiment is terminated.

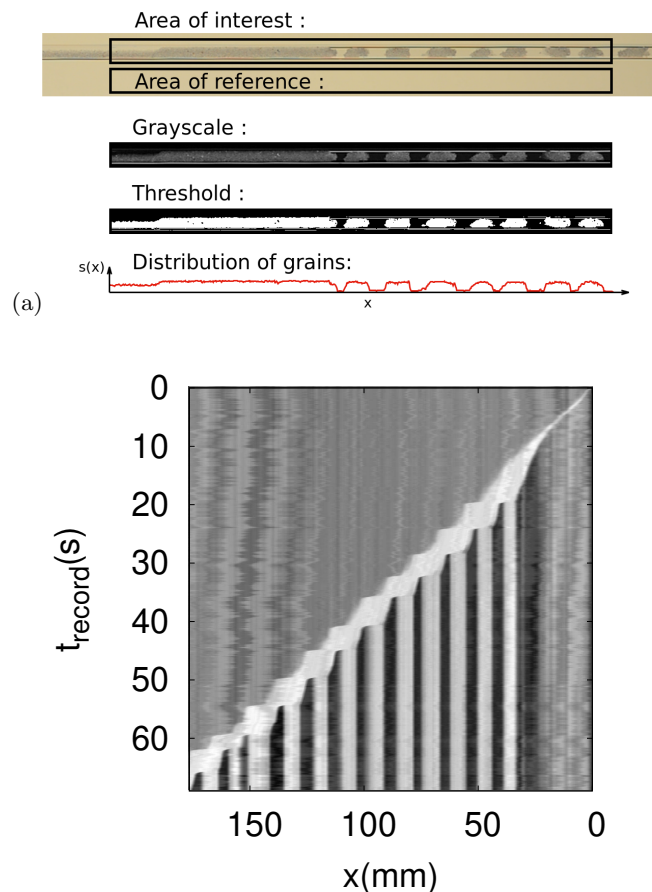
## Image processing

Images are recorded at 24 frames per second during the withdrawing of the water. The images are then cropped to the region of interest and converted to black and white, see Fig. 2 (a). Spatial and temporal variations in light intensity are corrected for by subtracting the background measured in an "area of reference" next to the tube, see on Fig. 2 (a). A threshold is then applied to isolate the granular matter and disregard the rest. A profile of granular matter along the tube  $s(x)$  is then obtained by summing the number of granular matter pixels in the perpendicular direction to the tube's axis. All these steps are illustrated on Fig. 2 (a). The temporal evolution of the granular profile is represented by means of a spatio-temporal diagram with the tube's axis  $x$  horizontally, and temporal axis vertically, developing downwards. The local value  $s(x)$  of the granular profile is then varying between a minimal value  $s_{min}$  when the granular matter is removed, and a maximal value  $s_{max}$  when the granular matter fills the entire tube's cross-section. The unperturbed sedimented granular matter corresponds to an intermediate value  $s_0$ . The granular profile values are rescaled into a grayscale map to produce a spatio-temporal diagram, see Fig. 2 (b).

## VISCOUS REGIME

### Fluidization of the sedimented granular matter

For withdrawing rates above  $10 \text{ mL min}^{-1}$ , the gas/liquid interface is clearly seen to move in a continuous manner, at a well defined speed  $v_0$ , see the spatio-temporal diagram in Fig 3(a). The speed is determined by the flow rate  $I_0$  and the geometry of the tube  $v_0 = 4I_0/(\pi D^2)$ . The total time of the experiment is then  $\tau = L_{tube}/v_0 = L_{tube}\pi D^2/(4I_0)$ . A growing fraction of the stationary sedimented granular material is bulldozed by the fast displacement of the interface and forms a fluidization front. Within the fluidization front the granular matter occupies the whole cross-section of the tube. The image analysis procedure identifies the fluidized granular material as regions with lighter gray levels. The spatio-temporal diagram in Fig. 3(a) shows the progress of the interface at a speed  $v_0$  as the boundary between darkest and lightest levels of gray, marking the boundary between the empty section of the tube and the fluidized granular material. This initial progress of the gas/liquid interface seems here slightly unsteady with a travelling speed decrease after  $t_{record} \approx 1.5 \text{ s}$ . Turning on the syringe pump might impose some transient elastic response from the tubing, which in turn affects the observed gas/liquid travelling speed. Note that for the flow rate values explored the flow regime is laminar with a Reynolds number value  $\leq 320$ .



(b)

FIG. 2. (a) Steps of image processing : (i) image cropping on the area of interest, (ii) grayscale image obtained after correcting fluctuations of illumination with an area of reference, (iii) threshold applied on the gray levels to isolate the granular material only, (iv) distribution of grains along the longitudinal  $x$ -axis. (b) Spatio-temporal diagram showing in grayscale the unperturbed sedimented granular matter (intermediate gray values), the packed granular matter (light values), and places where the granular matter is removed (dark values). The almost vertical and shivering stripes correspond to an artifact coming from light reflections on the glass tube.

### Effective viscosity in the fluidized front

The pressure response  $\Delta P(t)$  to the rapid withdrawal of the liquid reflects the viscous dissipation and the rheological properties of the mixture of water and sedimented granular matter at the imposed flow rate  $I_0$ . The initially sedimented granular material is gradually bulldozed up by the moving front of granular material which has been accumulated by the advancing meniscus. The front, consisting of densely packed but fluidized grains, advances at a speed  $v_{front} \geq v_0$  as indicated by the red triangles

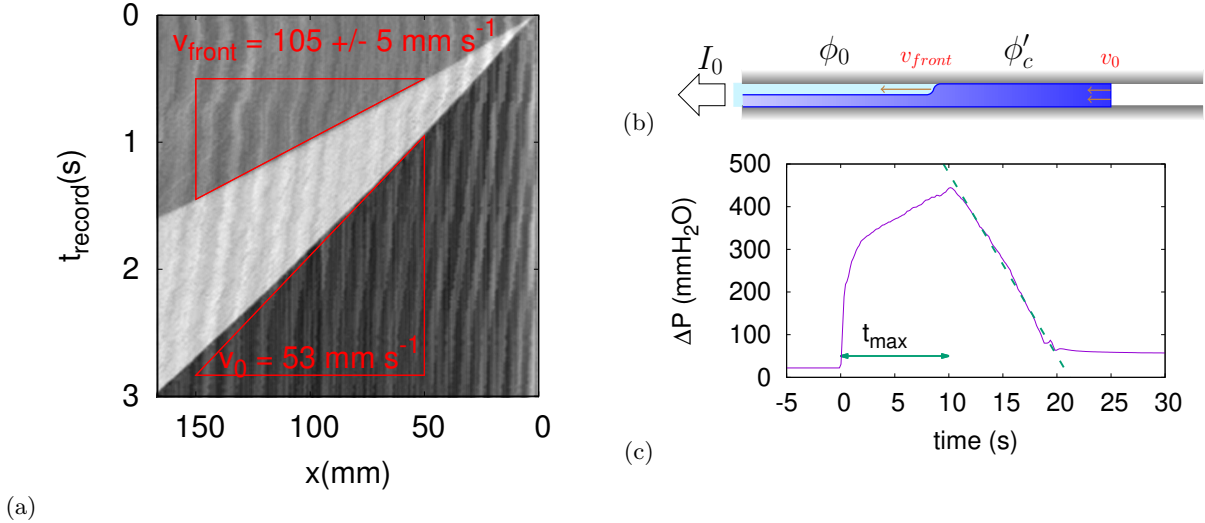


FIG. 3. (a) Spatio-temporal diagram focusing on the tube's open-end and recorded during the initial development of the fluidized front, corresponding to the time  $[0, 3]$ s in (c). The red triangles underline the fluidized front and gas/liquid interface speed. The same artifact as described in Fig. 2 (b) is visible here. The gas/liquid interface speed estimated from the imposed withdrawing rate and the tube's cross section is here  $v_0 = 4I_0/(\pi D^2) = 53 \text{ mm s}^{-1}$ . The fluidized front speed measured from this diagram is  $v_{front} = 105 \text{ mm s}^{-1} \pm 5 \text{ mm s}^{-1}$ . (b) Schematics of the millifluidic multiphase flow in the viscous regime. The fluidized front with filling fraction  $\phi'_c$  travels at speed  $v_{front}$  towards the sedimented granular material with filling fraction  $\phi_0$ . (c) Temporal evolution of the pressure imposed by the syringe pump during the gas/liquid interface displacement along the whole tube in viscous regime with a withdrawing rate  $I_0 = 10 \text{ mL min}^{-1}$ , beads size  $d_{beads} = [200, 300] \mu\text{m}$ , and an initial filling fraction  $\phi_0 = 0.33\phi_c$ .

in Fig. 3(a), and in the schematics in Fig. 3(b). By mass conservation we have  $\phi_0 v_{front} \Delta t = \phi'_c (v_{front} - v_0) \Delta t$  during  $\Delta t$ , with  $\phi'_c$  the filling fraction inside the fluidized front in reduced units. The speed ratio gives :

$$v_{front}/v_0 = \phi'_c/(\phi'_c - \phi_0) \quad (1)$$

which can be used to determine  $\phi'_c$ . A fluidized front of size  $L_s(t) = (v_{front} - v_0)t$  grows ahead of the travelling gas/liquid interface until it reaches the end of the tube. From this point the entire granular material contained in the tube is fluidized and exits until the experiment terminates.

A Hagen-Poiseuille law applied to the flow of a Newtonian fluid with viscosity  $\eta_0$  across a cylindrical geometry of length  $L$  and diameter  $D$  gives a pressure drop  $\Delta P = 128\eta_0 L I_0 / (\pi D^4)$ . The displacement of the gas/liquid interface along the tube implies that the remaining tube's length of water filling  $L(t) = L_{tube} - v_0 t$  decreases. If the tube was filled with water only, a linear decrease of pressure is expected, after some transient corresponding to the fast elastic response of the whole pumping system to the start-up of the pump. We observe instead a maximal value for the pressure drop at a time  $t_{max}$  after the start of the withdrawing, see Fig. 3 (c) with  $t_{max} \approx 10$ s. The time  $t_{max}$  corresponds to the time necessary for the fluidized front to reach the tube's outlet, when the whole granular material is suspended.

The time  $t_{max}$  satisfies  $v_{front} t_{max} = L_{tube}$ , which gives :

$$t_{max} = \frac{\phi'_c - \phi_0}{\phi'_c} L_{tube} \frac{\pi D^2}{4I_0}. \quad (2)$$

Eqs (1) and (2) provide two independent methods to estimate the filling fraction in reduced units in the fluidized front from image analysis (Fig. 3(a)) :

$$\phi'_c^{(SP)} = \phi_0 \frac{v_{front}/v_0}{v_{front}/v_0 - 1}, \quad (3)$$

and from the pressure signal (Fig. 3(b)):

$$\phi'_c^{(\Delta P)} = \phi_0 \frac{L_{tube} \pi D^2 / (4I_0)}{L_{tube} \pi D^2 / (4I_0) - t_{max}}. \quad (4)$$

From the spatio-temporal diagram on Fig. 3 (a)  $\phi'_c^{(SP)} \approx 0.66 \pm 0.035$ ; from the pressure signal on figure 3 (b)  $\phi'_c^{(\Delta P)} \approx 0.74 \pm 0.04$ . The granular material in the fluidized front shows here a significant compaction state compared to its initial filling fraction  $\phi_0 = 0.33$ , even if this level reaches approximately 66% to 74% of a loose random packing (at this compaction the suspension can still flow smoothly, although the effective viscosity has increased compared to the pure carrying fluid nominal viscosity value [8]). The two methods used to provide estimates of the filling fraction in the suspended front give a local value at the early stage of the withdrawal with

$\phi_c^{(SP)}$ , and a global value after averaging over the entire suspension front growth with  $\phi_c^{(\Delta P)}$ . This difference may explain the discrepancy between the two estimates as some transient initial elastic response of the setup are magnified with the former, and smoothed out with the latter.

After  $t_{max}$  the suspension is evacuated and the imposed pressure decreases with time. The Hagen-Poiseuille law here has to be considered with the effective viscosity of the suspension being larger than of a pure water,  $\eta_{eff} \geq \eta_0$ . The slope of the final pressure decrease for  $t \geq t_{max}$  is then determined by the effective viscosity  $\eta_{eff}$ :

$$\Delta P(t) = 128\eta_{eff}(L(t_{max}) - v_0t)I_0 \frac{4}{\pi D^4} \quad (5)$$

$$\frac{\partial \Delta P}{\partial t} = -128\eta_{eff} \left( \frac{4I_0}{\pi D^2} \right)^2 \frac{1}{D^2} \quad (6)$$

The equation (6) can be used to determine the effective viscosity  $\eta_{eff}$ . These values calculated from the pressure evolution during evacuation of the tube are summarized in Fig. 4 (a). We observe a decrease of the effective viscosity with larger flow rate, and the trend seems to follow the scaling  $\eta_{eff} \propto \eta_0 I_0^{-1.8}$ . This decrease with increasing values of the flow rate could be understood if we consider the evolution of the filling fraction in the fluidized front, for increasing values of the imposed withdrawing rate. The air/liquid interface bulldozing the initially sedimented granular matter is preceded by a fluidized front formed by suspended granular matter which progresses faster, see the spatio-temporal diagram in Fig. 3(a). Larger imposed withdrawing flow rates lead to the suspension of larger amounts of the initially sedimented granular material due to higher shear in the liquid phase. Suspended particles get further apart from each other and the filling fraction in the fluidized front decreases. Standard laws for the rheology of dense suspensions predict an increase of the effective viscosity of suspensions with the filling fraction, with a singularity at the maximal packing fraction, as in the Maron-Pierce correlation [33]:

$$\frac{\eta}{\eta_0} = (1 - \phi'_c/\phi_c)^{-2}. \quad (7)$$

If we input the scaling relation obtained from Fig. 4(a) we can estimate how the filling fraction in the fluidized front is expected to evolve with the imposed flow rate:

$$\phi'_c = 1 - \frac{I_0^{0.9}}{B} \quad (8)$$

with  $B \approx 41.5$ . It predicts a decrease of the filling fraction in the suspension as the flow rate increases, see the dashed line in Fig. 4(b). The symbols represent the filling fraction values  $\phi_c^{(\Delta P)}$  estimated from the time  $t_{max}$  on the imposed pressure curves, see Fig. 3(c). The experimental data points doesn't show a very satisfying agreement with the trend given by eq. (8). The error bars

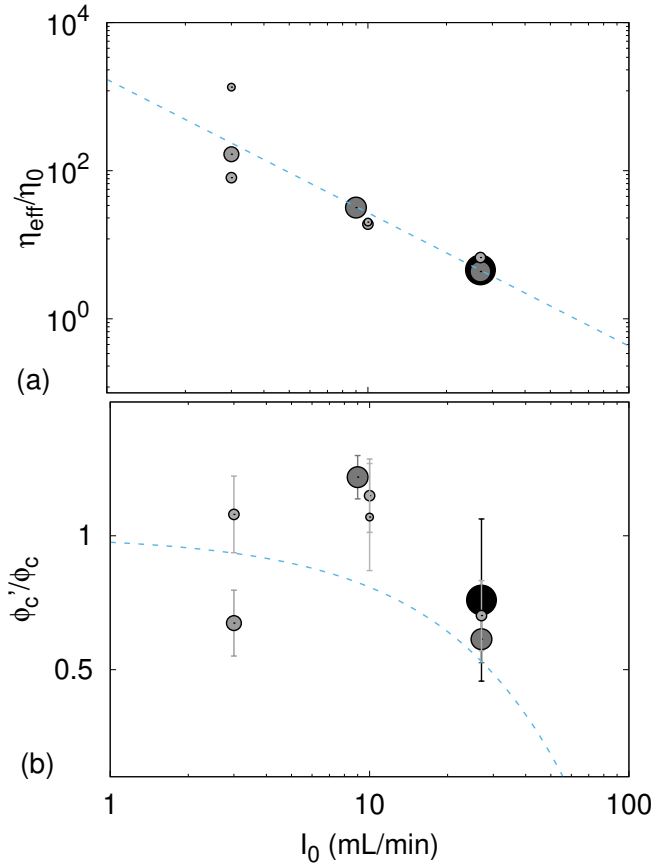


FIG. 4. (a) Effective viscosity  $\eta_{eff}$  normalized by the viscosity of water  $\eta_0$  and estimated from eq. (6), and (b) estimated filling fraction in the suspended front  $\phi_c^{(\Delta P)}$  in reduced units, versus withdrawing flow rate  $I_0$  in logscale. The filling fraction of the initially sedimented glass beads is  $\phi_0 = 0.5\phi_c$ . The dashed lines correspond (a) to the best linear fit in logscale  $\eta_{eff}/\eta_0 \propto I_0^{-1.8}$ , and (b) to the prediction obtained from the Maron-Pierce correlation with the previous fit used as an input. The shade and the size of the symbols gives from light to dark and from small to large respectively the beads sizes  $d_{beads} \in [53 - 75], [75 - 100], [100 - 150], [150 - 200]$  and  $[200 - 300]\mu\text{m}$ .

show the limited accuracy of the method for estimating the filling fraction in the suspension front.

## FRICTIONAL REGIME

### Plug size distribution

At low flow rates the granular material reorganizes into a series of plugs and gaps all along the tube. The gas/liquid interface is bulldozing the granular material which forms a growing accumulation front. At some point

the frictional interaction of the accumulation front with the confining boundaries becomes so large that a pore invasion process takes place and the gas percolates inside the accumulation front. The liquid in the accumulation front is displaced by the invading air and the granular packing gets partially drained. After a fraction of the accumulation front has been partially drained, it splits over the still fully immersed accumulation front, see the detail in Fig. 5(b). The gas/liquid meniscus continues to bulldoze the material ahead, leaving behind a static plug of partially saturated granular material. The repetition of this cyclic process runs all along the tube which contains a series of plugs at the end of the experiment, see Fig. 5 (a), and the spatio-temporal diagram in Fig. 2 (b). The image analysis of the final state, see Fig. 5 (a), has been used to extract quantitative information about how the plugs are distributed. Histograms of plugs and gaps size are obtained, see Fig. 5 (c), and the evolution of the average plug size obtained for different bead sizes is represented on Fig. 5 (d). No clear trend appears here and the plugs obtained have average sizes  $\langle L_{plug} \rangle = 7.7 \pm 3.1$  mm for all bead sizes used.

The average plugs size and gaps size is also measured as a function of the initial filling fraction for beads size  $d_{beads} \in [200 - 300] \mu\text{m}$ , see Fig. 5 (e). As expected the relative size of the gaps to the plugs is decreasing with the filling fraction. The series of plugs corresponds to the reorganization of the initially sedimented granular material, maintaining the initial filling fraction of granular material  $\phi_0$  (fraction of cross-sectional area occupied by sedimented grains). Large gaps compared to plugs are then expected when the initial filling fraction is small. Small gaps are expected when the initial filling fraction is large, as the large amount of granular material occupies a large fraction of the available space. Fig. 5 (e) shows that the plug size is almost constant with the initial filling fraction of grains in the tube. The gaps sizes accommodate then most of the filling fraction changes. The conservation of the filling fraction after reorganization of the granular material into a series of plugs leads to rewrite the initial filling fraction as  $\phi_0 = L_{plug} / (L_{plug} + L_{gap})$ . An assumption that the plug size  $L_{plug}^0$  is independent of filling fraction leads to a good estimate of the gap size as a function of  $\phi_0$  :

$$L_{gap} = L_{plug}^0 \left( \frac{1}{\phi_0} - 1 \right), \quad (9)$$

see the dashed line on the Fig. 5 (e).

### Permeability generated

The measurements of the pressure imposed by the pump at low flow rate exhibit a sawtooth shaped behaviour. The pressure slowly increases until a maximal value is reached before it drops quickly, see Fig. 6 (a)

(inset). On top of these fluctuations, an increasing trend is observed, see the uncorrected signal on Fig. 6 (a) with black line. It is an effect of the viscous dissipation of the gas flow across a growing number of plugs formed. The pressure imposed by the pump can be decomposed into two contributions: (i) The cyclic bulldozing and plug splitting events correspond to a stick-slip dynamics leading to the sawtooth shape; (ii) The flow of air across the growing number of plugs formed generates an increasing viscous dissipation with time, which corresponds to the global pressure increase. A global correction is then applied to remove the contribution from the air flow by considering the total pressure increase  $\Delta P(t_{end})$  measured at the end of the plugs formation process, see Fig. 6(a). The pressure increase due to the viscous dissipation of the air flow across the formed plugs is assumed to follow a linear trend  $\Delta P(t) = \Delta P(t_{end})t/t_{end}$ . The frictional dissipation is then assumed to contribute as  $\Delta P_{fric}(t) = \Delta P_{measured}(t) - \Delta P(t_{end})t/t_{end}$ . We estimate the permeability of the total plugs series  $k_{plugs}^{tot}$  to air flow by means of a Darcy law :

$$\Delta P(t_{end}) = 4\eta_{air}I_0 \sum_i L_{plug}^{(i)} / (k_{plugs}^{tot} \pi D_{tube}^2), \quad (10)$$

with  $\eta_{air}$  the viscosity of air, and the total final plug length sum  $\sum_i L_{plug}^{(i)} = \phi_0 L_{tube}$ , which is determined by the initial filling fraction  $\phi_0$  as if all plugs formed were end-to-end all together. The gaps between two plugs are not assumed to contribute significantly to the measured pressure drop. For a granular packing made of beads of diameter  $d_{beads}$ , and packed with a filling fraction  $\varphi_c$ , the Carman-Kozeny equation gives an idealized estimate of the permeability  $k_0 = (d_{beads}^2/180)(1 - \varphi_c)^3/\varphi_c^2$ . The approximated permeability for glass beads in the range  $[200 - 300] \mu\text{m}$  with a packing fraction  $\varphi_c$  is then  $k_{0,250} \approx 1.5 \times 10^{-7} \text{ cm}^2$ , which gives the same order of magnitude as for the experimental measurements reported in the past for gaseous flows across a porous media formed by a packing of glass beads of similar sizes [28, 34, 35]. The Figure 6(b) gives the ratio of the measured plugs permeability  $k$  to the ideal permeability  $k_0$ . The number of ideal geometrical pathways visited by the flow of air through the plugs series appears to be strongly reduced. The flow of air across formed plugs seems to follow only 5 to 60% of the geometrical pathways. This is most likely related to the partial saturation of the formed plugs. During the drainage process a fraction of the total water contained in the granular packing remains in the plug. The water is trapped with no possibility to escape after the splitting, which is obstructing a fraction of the interstitial voids, and reduces the permeability of the plugs. Small beads size seem to increase the trapping of water.

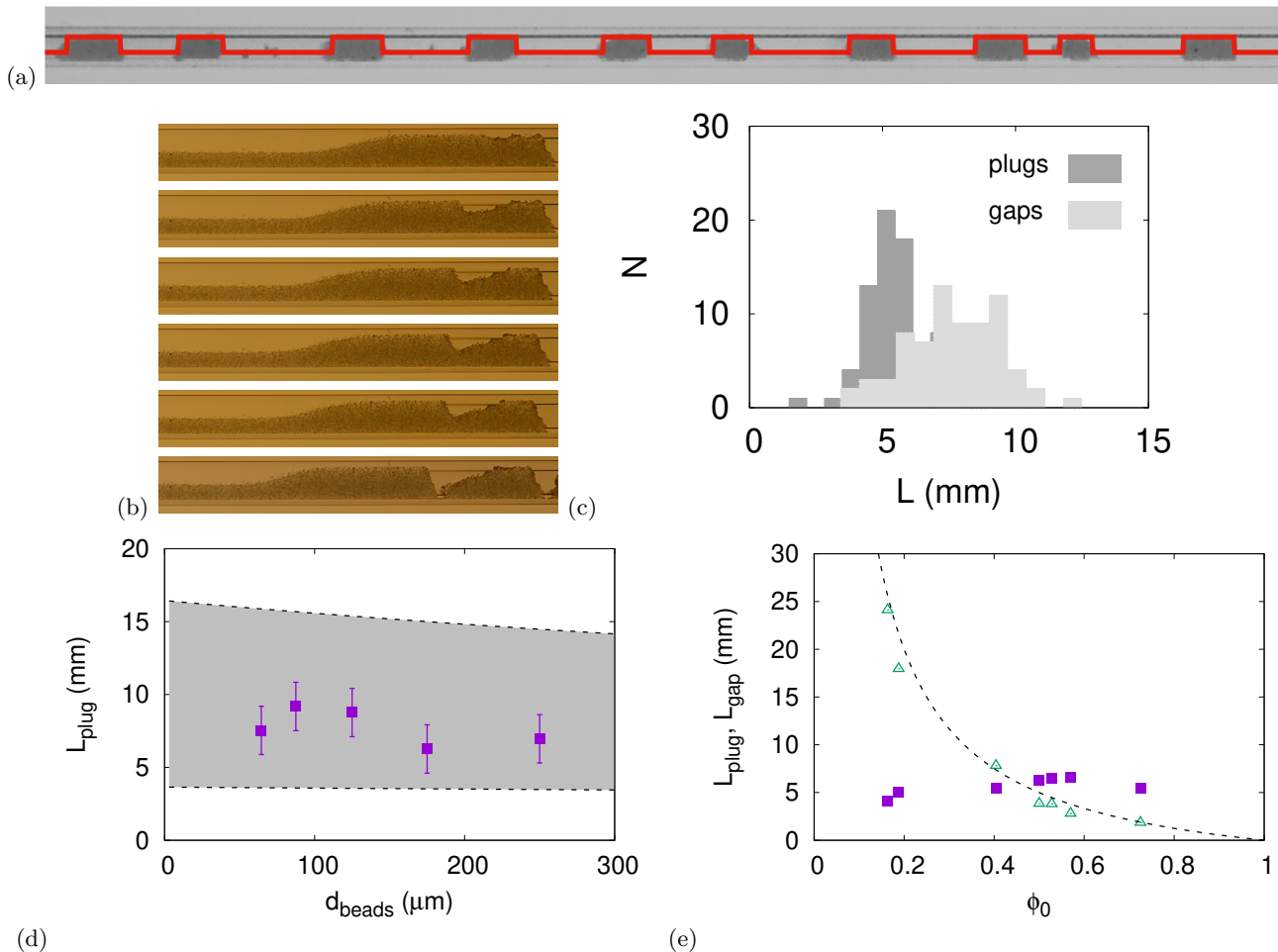


FIG. 5. (a) Detail of the final series of plugs obtained with beads size  $d_{beads} \in [200 - 300]\mu\text{m}$ , after pumping out water at a flow rate  $I_0 = 0.3 \text{ mL}\cdot\text{min}^{-1}$ . The initial filling fraction used here is  $\phi_0 = 0.4\phi_c$ . The red line corresponds to the square signal measuring the idealized granular material profile along the tube. The scale is given here by the external diameter of the tube which is 4 mm. (b) Detail of the formation of one plug. (c) Histogram representing the distribution of plugs size (dark gray), and gaps size (light gray) for the observation reported in (a). (d) Average plug size measured as a function of beads size (solid squares, error bars measure the largest difference obtained for the same beads size). The two dashed lines are bounding the domain covered by the semi-analytical predictions based on eq (17) with  $\alpha \in [0.1, 0.6]$ ,  $\lambda = 7.2 \text{ mm}$ ,  $\kappa = 0.7$ ,  $\sigma_g = 4.5 \text{ Pa}$ , and  $P_{pore} = \gamma/d_{pore}$ , with  $\gamma = 72 \times 10^{-3} \text{ Pa}\cdot\text{m}$  and  $d_{pore}$  from Fig. 7 (b). (e) Evolution of the average plugs size (solid squares), and gaps size (open triangles) as function of the initial filling fraction  $\phi_0$  for beads size  $d_{beads} \in [200, 300] \mu\text{m}$ . The dashed line shows the expected trend for gap size with a fixed value for plugs  $L_{plug}^0 = 5 \text{ mm}$ .

### Pressure variations

As we mentioned above, during the formation of the series of plugs the pressure shows a typical sawtooth shape. Slow increases of pressure stop at a peak value  $P_{max}$ , before a sudden pressure drop  $\Delta P$ , see on Fig. 6(b). After correcting the pressure measurement, the maximal pressure values are fluctuating around an average value  $\langle P_{max} \rangle$  as shown in Fig. 7(a). The maximal pressure increases as the beads sizes decreases. This trend is consistent with the decreasing pore sizes obtained with finer particles. The interstitial space between glass beads being smaller with smaller beads, the pressure necessary to

bend the gas/liquid interface into the granular accumulation front increases. The characteristic pore size  $d_{pore}$  has been estimated by making use of the Laplace law  $P_{max} = 4\gamma/d_{pore}$ , and is represented in Fig. 7(b) for various bead sizes.

### Janssen stress structure

The formation of the series of granular plugs is a cyclic process that can be decomposed into three steps :

*Step 1 - Capillary bulldozing :* The stress is imposed by the syringe pump into the system, the gas/liquid interface transfers the stress towards the granular mate-

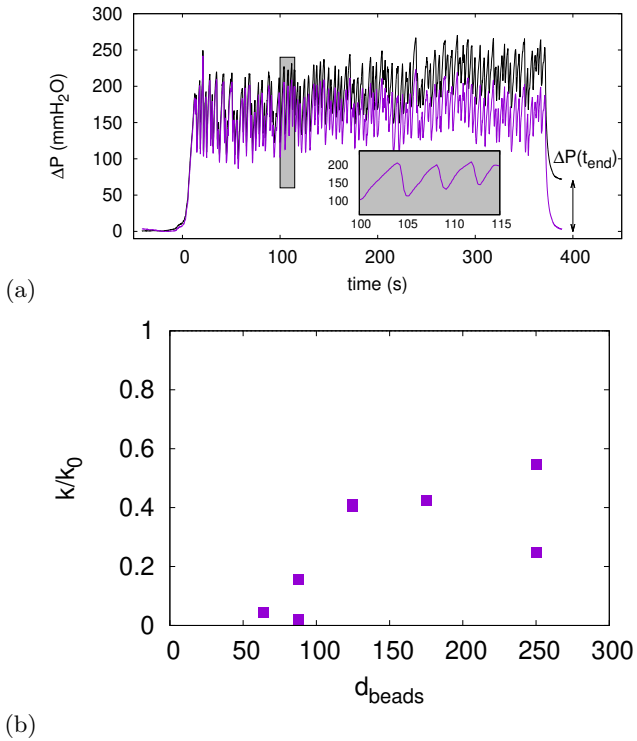


FIG. 6. (a) Measurement of the pressure imposed by the syringe pump during the formation of plugs dominated by frictional dissipation (black line), and after correcting the viscous dissipation of air flow across the plugs already formed (purple line). A withdrawing rate  $I_0 = 0.3 \text{ mL min}^{-1}$  is imposed here with glass beads of diameter  $d_{beads} \in [200 - 300] \mu\text{m}$ . The inset shows the zoom over the part of corrected signal highlighted with the greyed rectangle. (b) Average value of the effective permeability of individual plugs formed, normalized by the geometrical permeability determined by the beads size and the Carman-Kozeny formula.

rial which responds by a frictional displacement. As the gas/liquid interface moves, a front of accumulated granular material increases, and so does the frictional stress.

*Step 2 - Drainage :* At some point the pressure required to sustain the frictional displacement becomes larger than the pore entry pressure  $P_{pore}$  of the compacted granular material. It corresponds to the Laplace pressure across a curved meniscus between the grains so  $P_{pore} = 4\gamma/d_{pore}$  where  $\gamma$  is the surface tension of the gas/liquid interface, and  $d_{pore}$  the pore size. Once the pressure imposed by the syringe pump has reached this value, the gas/liquid interface enters the granular material and a drainage process takes place.

*Step 3 - Split and slip :* The fast drainage process by pore invasion ends when the partially drained section of the accumulation front splits from the rest, and is left as a static plug in the tube. The splitting occurs after enough compacted granular material is drained so that the frictional interaction with the confining walls is reduced. The still immersed granular material

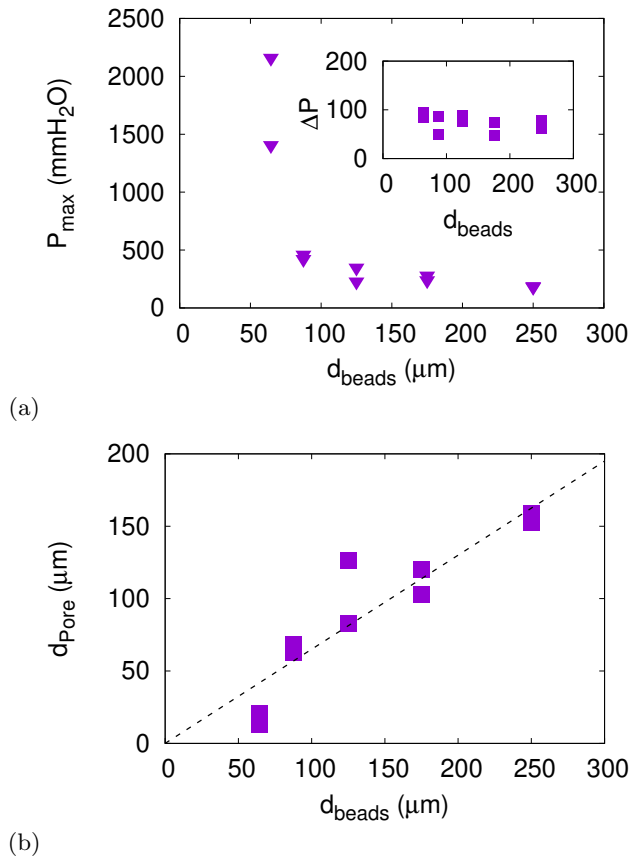


FIG. 7. (a) Average maximal pressure peak  $P_{max}$  and (inset) pressure drop  $\Delta P$  values as function of bead size  $d_{beads}$ . (b) Effective pore diameter  $d_{pore}$  corresponding to the average maximal pressure  $P_{max}$  as a function of bead size  $d_{beads}$ . The dashed line gives a slope  $d_{pore} = 0.65 d_{beads}$ .

can then be bulldozed further. Once the plug has split the pressure is reduced by the viscous slip of the accumulation front, before a next frictional displacement takes place.

The drainage and plug splitting is captured by the series of close-ups on Fig. 5(b).

*Janssen's model* As the capillary interface slowly bulldozes the sedimented granular material, a granular front of packed beads develops. The granular material slowly compactifies, and the contacts between the grains form force chains which are distributing the stress applied by the interface. We can establish a force balance on a slice  $dx$  of the compacted accumulation front, see Fig. 8(a):

$$\frac{\pi D^2}{4} \sigma_{xx}(x) - \frac{\pi D^2}{4} \sigma_{xx}(x + dx) - \pi D dx \sigma_w(x) = 0. \quad (11)$$

The dynamics is here assumed to be quasi-static. A resistive tangential stress at the tube's wall  $\sigma_w(x)$  is considered. It takes into account the contributions from

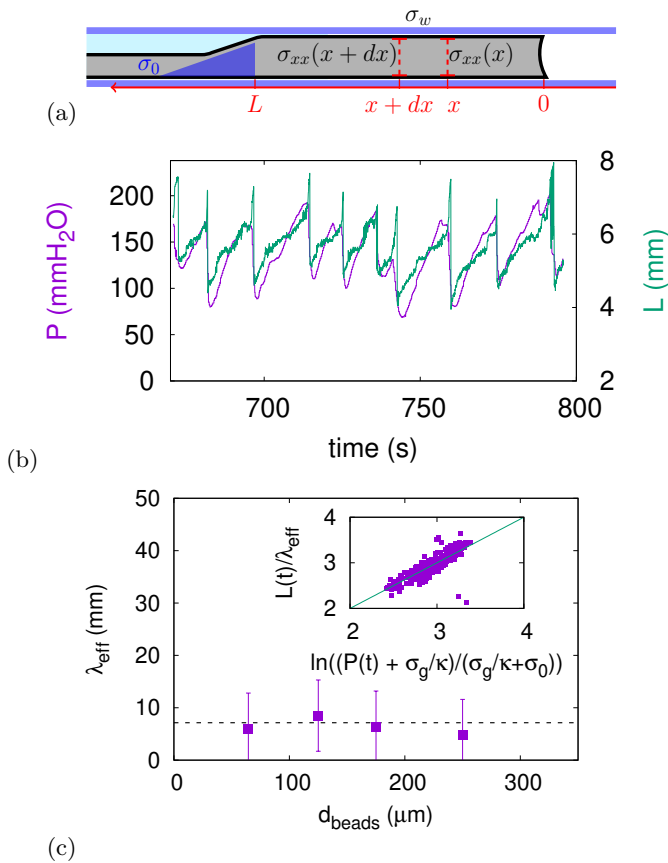


FIG. 8. (a) Schematics illustrating the force balance considered to extract the Janssen’s length scale. (b) Detail of the pressure  $P$  and accumulation front length  $L$  time series for  $d_{\text{beads}} \in [200, 300] \mu\text{m}$ , and with a withdrawing flow rate  $I_0 = 0.1 \text{ mL min}^{-1}$ . (c) Janssen’s length scale best fitted value  $\lambda_{\text{eff}}$  as a function of beads size  $d_{\text{beads}}$ . The dashed line corresponds to the mean frictional length  $\langle \lambda_{\text{eff}} \rangle = 7.2 \text{ mm}$ . The inset shows the linear fit for  $L(t)/\lambda_{\text{eff}}$  following eq. (14), obtained in the same experimental conditions as stated in (b).

the stress redirection due to the Janssen’s law  $\sigma_{rr}(x) = \kappa \sigma_{xx}(x)$ , and from the weight of the granular material slice  $\sigma_g = \varphi_c \Delta \rho g D / 4$ . The force balance results in an Ordinary Differential Equation :

$$\frac{d\sigma_{xx}}{dx} + \frac{4}{D} \mu \kappa \left( \sigma_{xx}(x) + \frac{\sigma_g}{\kappa} \right) = 0, \quad (12)$$

with a solution written as:

$$\sigma_{xx}(x) + \sigma_g/\kappa = (\sigma_0 + \sigma_g/\kappa) \exp[(L - x)/\lambda]. \quad (13)$$

We have introduced here the notation  $\lambda = D/(4\mu\kappa)$  for the frictional length. The longitudinal stress vanishes after a certain distance  $L$  from the bulldozing capillary interface. The longitudinal stress boundary condition at this point is denoted  $\sigma_0$ . It originates from the gravitational stress on the glass beads bounding the compacted granular front, see the blue profile on Fig. 8(a). For the sake of simplification we are using the approx-

imation  $\sigma_0 \approx \mu\sigma_g$  in all the following numerical estimates. A more detailed modelling is reported in [32] which takes into account a more accurate wedge-shaped retaining profile with tangential interaction with the confining walls, and the shearing into the unperturbed sedimented granular material. With our parameters it gives a corrective prefactor of  $\approx 1.2$  which we have decided to neglect in this study.

As the gas/liquid interface progresses the sedimented granular material accumulates into a growing compaction front. The image processing of each experiment provides the time evolution of the compaction front length  $L(t)$ . On Fig. 8(b) we have plotted the synchronized pressure imposed by the pump  $P(t)$  and the length of the compaction front  $L(t)$  during several plug formations. The compaction front length increases together with the imposed pressure. This trend is consistent with the Janssen’s model which assumes an exponential growth of the imposed pressure with  $L$ . The pressure driving the gas/liquid interface is given by the eq (13) at  $x = 0$  :

$$P(t) = (\sigma_0 + \sigma_g/\kappa) \exp(L(t)/\lambda) - \sigma_g/\kappa. \quad (14)$$

A sharp increase in  $L$  can be observed just before each slip, which is an artifact coming from the length estimation scheme. For some few points in every cycle our algorithm is not able to distinguish the drained section from the still-immersed accumulation front, both appearing with a maximal filling fraction without air gap in between (see the three top pictures in the close-up detail of one plug formation in Fig. 5(b)). Each sharp increase in  $L$  corresponds to the total length of the drained plug about to detach, added to the immersed accumulation front.

On the Fig. 8(c) (inset) we use the pressure  $P(t)$  and accumulation front length  $L(t)$  time-series to plot  $L(t)/\lambda_{\text{eff}}$  as a function of  $\ln[(P(t) + \sigma_g/\kappa)/(\sigma_g/\kappa + \sigma_0)]$ , for a withdrawing rate  $I_0 = 0.1 \text{ mL min}^{-1}$  and beads size  $d_{\text{beads}} \in [200 - 300] \mu\text{m}$ . We use the frictional parameter value  $\kappa = 0.7$  to estimate  $\sigma_g/\kappa$ . We obtain a linear relationship and the parameter  $\lambda_{\text{eff}}$  is adjusted to match the equation (14). The best fitting values for  $\lambda_{\text{eff}}$  is represented on Fig.8(c) for every beads sizes, with an average value  $\langle \lambda_{\text{eff}} \rangle = 7.2 \text{ mm}$ . Such a value for the frictional length obtained with a Janssen’s coefficient  $\kappa = 0.7$  [21, 22, 32], indicates an effective frictional coefficient  $\mu_{\text{eff}} = 0.1$ . This value appears quite low compared to standard glass-glass friction coefficients. A low friction coefficient maybe due to lubrication and rolling effects that the present model do not take into account. In addition, the experimental error bars considered for  $\lambda_{\text{eff}}$  opens the possibility to consider smaller frictional length values, which would in turn correspond to larger frictional coefficients.

### Plug size prediction

Modelling the frictional stress inside the accumulation front can be used to explain the observed plug length evolution with beads size showed on Figure 5(d). The pore invasion step, prior to the plug splitting in the cyclic process structuring of the confined granular matter, starts when the pressure imposed by the syringe pump reaches the pore pressure value  $P_{pore}$ , at this stage the size of the accumulation front  $L_{max}$  can be obtained from equation (14) :

$$P_{pore} = (\sigma_0 + \sigma_g/\kappa) \exp(L_{max}/\lambda) - \sigma_g/\kappa. \quad (15)$$

The pore invasion process drains away a fraction  $\alpha = k/k_0$  of the water saturating the accumulation front, see Fig. 6(b). The flow of air invading the packed granular material is observed close to the top side of the tube, so that one can assume that the top fraction  $\alpha$  of the cross sectional area of the packing is getting drained. At the forefront of the invading air phase, a hydrostatic pressure force  $(\alpha\pi D^2/4)P_{pore}$  is acting on the compacted grains forming the accumulation front. The length of the accumulated front length ahead of the invading air phase is decreasing, until the air phase has progressed over a distance  $L_{plug}$  inside the packing, when a next slip becomes possible. The hydrostatic pressure force applied at the forefront of the air phase invasion, on a reduced cross section of the granular packing, overcomes then the frictional resistance of the still immersed accumulated front ahead :

$$\alpha P_{pore} = (\sigma_0 + \sigma_g/\kappa) \exp\left(\frac{L_{max} - L_{plug}}{\lambda}\right) - \sigma_g/\kappa. \quad (16)$$

From that moment the still immersed granular material experiences a next bulldozing from capillary forces, while the partially drained part forms a static plug permeable to air flow. Combining eqns (15) and (16) helps to provide an estimate for  $L_{plug}$  :

$$\frac{L_{plug}}{\lambda} = \ln\left(\frac{P_{pore} + \sigma_g/\kappa}{\alpha P_{pore} + \sigma_g/\kappa}\right) = \ln\left(\frac{1 + F}{\alpha + F}\right). \quad (17)$$

This relationship brings out a dimensionless number  $F = \sigma_g/(\kappa P_{pore})$  measuring the ratio between gravitational to capillary stresses in the confined granular phase. Capillary stresses must be large enough compared to gravitational to allow for a bulldozing, and in our experiment  $F \approx 10^{-5}$  so that this condition is satisfied.

This prediction of the plug length is then mostly dependent on the estimation of the fraction  $\alpha$  of removed water from the accumulation front after drainage. Based on the observations in Fig. 6(b) we have considered a range  $\alpha \in [0.1, 0.6]$  and calculated the corresponding range of plug sizes thanks to eq. (17) as a function of beads

size  $d_{beads}$ . We obtained the greyed area in Fig. 5(d), for the measured pore pressure values  $P_{pore}$  reported on Fig. 7(a). The frictional parameters  $\kappa = 0.7$  have been used, and the effective frictional length  $\lambda = 7.2\text{mm}$  from Fig. 8(c). This analytical prediction encompasses the experimental observations, but could be improved with more accurate measurements of  $\alpha$ .

### TRANSITION

A phase diagram had been established [1] to distinguish the two different displacement regimes obtained when the flow rate  $I_0$  and the glass beads's size  $d_{beads}$  were varied, see Fig. 9. The viscous regime is observed for large values of flow rate, and requires larger flow rate values for larger glass beads. On the contrary the frictional regime is observed for small values of flow rate, and is visible for slightly smaller flow rate values for smaller glass beads. In between the two main regimes, a third transitional regime can be observed for a range of intermediate flow rate values. In this transitional regime some plugs are formed irregularly, together with the propagation of a fluidized front. A frictional dimensionless number :

$$N = \frac{\delta P_{visc}}{\delta P_{fric}} \quad (18)$$

had also been introduced and tested to predict the transition between the frictional and viscous regimes of displacement [1]. Here we are using it to estimate the stable formation of one plug subject to the viscous drag corresponding to the flow rate  $I_0$  by focusing on the stability of a slice  $\delta L$  of an accumulation front. The viscous stress exerted on an accumulation front of size  $\delta L$  can be derived from the Darcy's law :

$$\delta P_{visc} = \frac{\eta}{k_0} \frac{4I_0}{\pi D^2} \delta L. \quad (19)$$

with the liquid viscosity  $\eta$ , the flow rate  $I_0$ , the permeability  $k_0$ , the size of confinement  $D$ . The permeability can be estimated from the Carman-Kozeny equation as above. The frictional resistance of an accumulation front of size  $L$  has been estimated in eq. (14), which gives for an accumulation front of size  $\delta L$  :

$$\delta P_{fric} = (\sigma_0 + \sigma_g/\kappa) \exp(\delta L/\lambda) - \sigma_g/\kappa. \quad (20)$$

Large flow rates leading to viscous stresses larger than the frictional resistance (20) do not allow the formation of an accumulation front of size  $\delta L$ .

Eqs. (19) and (20), combined together for a unity value of the frictional number defined in (18), give a maximal flow rate value compatible with a plug formation of size  $\delta L$ , i. e. when frictional and viscous dissipation are of similar magnitude :

$$I_{0,N=1} = \frac{k_0 \pi D^2}{4\eta \delta L} [(\sigma_0 + \sigma_g/\kappa) \exp(\delta L/\lambda) - \sigma_g/\kappa]. \quad (21)$$

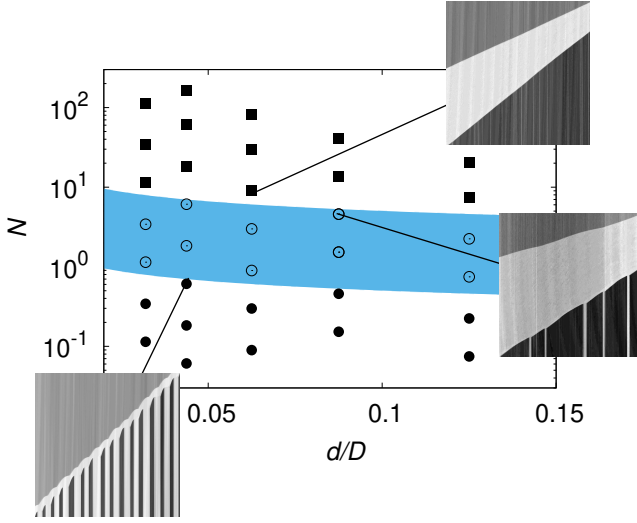


FIG. 9. Phase diagram showing the three different multi-phase flow regimes when the rescaled grains size  $d_{beads}/D$  and the frictional number  $N$  are varied. The following frictional parameters are used here to calculate  $N$ :  $\delta L = 5\lambda$ ,  $\lambda = \langle \lambda_{eff} \rangle$ ,  $\kappa = 0.7$ ,  $\varphi_c = 0.6$ ,  $\Delta\rho = 1.463 \times 10^3 \text{ kg m}^{-3}$ . A viscous dissipation regime is observed for large values of the frictional number  $N \geq 10$  (solid square), whereas a solid friction dissipation regime is observed for small values  $N \leq 1$  (solid disk). Intermediate frictional number values  $N \in [1, 10]$  corresponds to intermediate displacement regimes exhibiting characteristics from both regimes with plug formation and growing suspension front (open circle). The blue shaded area covers the transitional regime with the empirical scaling  $N \propto (d_{beads}/D)^{-0.4}$ . Insets show spatio-temporal diagrams obtained in the central part of the tube showing the gas/liquid interface displacement from right to left with the longitudinal axis horizontally and the time axis developing downwards, at flow rate  $I_0 = 3 \text{ mL min}^{-1}$  and beads size  $d_{beads} \in [100 - 150] \mu\text{m}$  (viscous regime),  $I_0 = 3 \text{ mL min}^{-1}$  and beads size  $d_{beads} \in [150 - 200] \mu\text{m}$  (transitional regime), and  $I_0 = 0.1 \text{ mL min}^{-1}$  and beads size  $d_{beads} \in [75 - 100] \mu\text{m}$  (frictional regime).

In Fig. 9 we can observe the transition between the two regimes dominated by viscous and frictional dissipation respectively at large and low values of the frictional number. To calculate  $N$  from eqs. (18), (19) and (20), we used the following frictional parameters  $\kappa = 0.7$  and  $\mu_{eff} = 0.1$  derived from the mean frictional length  $\langle \lambda \rangle = 7.2 \text{ mm}$  estimated on Fig. 8 (c). It appears that an accumulation front size  $\delta L \approx 5\lambda$  must be considered to get a unity values of the frictional number when the viscous regime crosses over to the frictional regime. The blue shaded area covers the transitional regime with an empirical scaling  $N \propto (d_{beads}/D)^{-0.4}$ .

## CONCLUSION

In this paper we are reporting a detailed investigation on how a sedimented granular material immersed in water and confined in an horizontal millifluidic tube responds to the displacement of an air/water interface. The meniscus is bulldozing the initially sedimented granular material following two different regimes determined by the flow rate  $I_0$  imposed in the tube, and the beads size  $d_{beads}$  of the granular material used.

A large imposed flow rate leads to large displacement speed of the meniscus. The sedimented granular material gets fluidized as the interface approaches and a fluidized front develops ahead. We performed measurements of the pressure imposed by the syringe pump  $P(t)$ . We explained the non-monotonous evolution of the pressure difference by modelling the propagation of a fluidized front perturbing the sedimented granular bed, and then the discharge of the fluidized granular material out of the tube. The study of the pressure difference  $\Delta P$  required to impose the given flow rate  $I_0$  has shown that the effective viscosity  $\eta_{eff}$  in the fluidized front is a decreasing function of  $I_0$ .

A small imposed flow rate leads on the contrary to a small displacement speed of the meniscus. The sedimented granular material is slowly bulldozed by the progressing meniscus, and a cyclic process takes place, decomposed into (i) the slow accumulation of a granular front, (ii) the rapid drainage of the water through a section of the accumulation front once the pore pressure is reached, and (iii) the granular plug splitting and a quick viscous dissipation before the slow accumulation starts again. This leads to the re-structuring of the initially sedimented granular material into a series of granular plugs left in the tube once the meniscus finishes its progression.

The average size of the plugs and the gaps is consistent with a mass conservation of the granular material inside the tube. This confirms that the progress of the meniscus has re-organized the initially sedimented granular material. An observation done for glass beads of diameter  $d_{beads} \in [200 - 300] \mu\text{m}$  has shown that the average plugs size is nearly constant whatever the initial filling fraction. The size of the plugs formed seems even to be independent of the beads sizes with  $L_{plugs} \in [6, 10] \text{ mm}$ .

The pressure variation during the plug formation process has a typical sawtooth shape which is a signature of an underlying stick-slip process. The maximal pressure peak reached before the rapid drainage and plug splitting has been used to estimate the pore sizes in the accumulation front.

The evolution of the pressure variations with the obtained plug size distribution has been also interpreted by means of the Janssen's model. A typical frictional length  $\lambda \approx 7.2 \text{ mm}$  appears in the evolution of the pressure required to slowly bulldoze the accumulation front,

independent of the beads sizes.

A predicting model for the transition from a viscous to a frictional dissipation regimes has also been proposed with a dimensionless frictional number  $N$ . It can be used to provide an estimate of the critical flow rate as a function of the beads size; the density contrast between the granular material and the liquid; the viscosity of the liquid. Further experimental characterizations should however be considered to test and improve the robustness of the present prediction over the whole set of parameters. In particular measuring the critical flow rates for different density contrasts by making use of beads formed out of different materials would probably be the next step. Similarly, changing the viscosity of the fluid phase by mixing water with glycerol in different concentrations could also be considered.

The generality of the here documented physical phenomena could also be inferred from changes of the granular matter wettability. At the interface, the wettability will mostly impact the maximal pore pressure  $P_{pore}$ . For hydrophobic beads an interesting mirror-experiment could be conducted with a dry sedimented hydrophobic granular matter bulldozed by a progressing water interface. We are expecting then to find the same displacement regimes, with a structuring of the granular phase into plugs when the solid friction dominates, and a fluidization regime when the viscous dissipation in the gas phase dominates, at very high imposed flow rate most likely.

The present work has been conducted on a specific horizontal tube-flow configuration. It possesses an interest for the handling of complex so-called frictional fluids in geometrical confinements, such as innovative catalytic processes [36], or waste water or biomass slurries management [37, 38]. We provide here observations and discussions about competing or collaborative effects of viscosity, solid friction and capillarity leading to diverse flow behaviours ranging from non-Newtonian rheological properties to pattern formation.

This work was supported by the Research Council of Norway through its Centres of Excellence funding scheme, project number 262644 for the Porous Media Laboratory. BS acknowledges support from the Ser Cymru National Research Network in Advanced Engineering and Materials, NRN141.

- 
- [1] G. Dumazer, B. Sandnes, M. Ayaz, K. J. Måløy, and E. G. Flekkøy, Frictional fluid dynamics and plug formation in multiphase millifluidic flow, *Phys. Rev. Lett.* **117**, 028002 (2016).
- [2] A. Costa, and G. Macedonio, Nonlinear phenomena in fluids with temperature-dependent viscosity: An hysteresis model for magma flow in conduits, *Geophys. Res. Lett.* **29**, 40-1 (2002).

- [3] A. Berti, Phase separation in lava flow, *Eur. J. Mech. B* **45**, 84 (2014).
- [4] D. Gidaspow, and J. Huang, Kinetic theory based model for blood flow and its viscosity, *Ann. of Biomed. Eng.* **37**, 1534 (2009).
- [5] J. B. Freund, and M. M. Orescanin, Cellular flow in a small blood vessel, *J. Fluid Mech.* **671**, 466 (2011).
- [6] Z. Shen, T. M. Fischer, A. Farutin, P. M. Vlahovska, J. Harting, and C. Misbah, Blood crystal: Emergent order of red blood cells under wall-confined shear flow, *Phys. Rev. Lett.* **120**, 268102 (2018).
- [7] R. Mari, R. Seto, J. F. Morris, and M. M. Denn, Shear thickening, frictionless and frictional rheologies in non-Brownian suspensions, *J. Rheol.* **58**, 1693 (2014).
- [8] J. J. Stickel and R. L. Powell, Fluid mechanics and rheology of dense suspensions, *Annu. Rev. Fluid Mech.* **37**, 129 (2005).
- [9] M. M. Denn, and J. F. Morris, Rheology of non-Brownian suspensions, *Annu. Rev. Chem. Biomol. Eng.* **5**, 203 (2014).
- [10] R. P. Behringer, D. Bi, B. Chakraborty, A. Clark, J. Dijkstra, J. Ren, and J. Zhang, Statistical properties of granular materials near jamming, *J. Stat. Mech.* P06004 (2014).
- [11] E. Brown, and H. M. Jaeger, Shear thickening in concentrated suspensions: phenomenology, mechanisms and relations to jamming, *Rep. Prog. Phys.* **77**, 046602 (2014).
- [12] A. Fall, F. Bertrand, D. Hautemayou, C. Mezière, P. Moucheront, A. Lemaître, and G. Ovarlez, Macroscopic discontinuous shear thickening versus local shear jamming in cornstarch, *Phys. Rev. Lett.* **114**, 098301 (2015).
- [13] E. Rabinovich, and H. Kalman, Flow regime diagram for vertical pneumatic conveying and fluidized bed systems, *Powder Technol.* **207**, 119 (2011).
- [14] E. V. J. Manjula, W. K. Hiromi Ariyaratne, C. Ratnayake, and M. C. Melaaen, A review of CFD modelling studies on pneumatic conveying and challenges in modelling offshore drill cuttings transport, *Powder Technol.* **305**, 782 (2017).
- [15] R. Naveh, N. M. Tripathi, and H. Kalman, Experimental pressure drop analysis for horizontal dilute phase particle-fluid flows, *Powder Technol.* **321**, 355 (2017).
- [16] R. Lenormand, E. Touboul, and C. Zarcone, Numerical models and experiments on immiscible displacements in porous media, *J. Fluid Mech.* **189**, 165 (1988).
- [17] B. Zhao, C. W. MacMinn, and R. Juanes, Wettability control on multiphase flow in patterned microfluidics, *PNAS* **113**, 10251 (2016).
- [18] G. Løvoll, Y. Méheust, R. Toussaint, J. Schmittbuhl, and K. J. Måløy, Growth activity during fingering in a porous Hele-Shaw cell, *Phys. Rev. E* **70**, 026301 (2004).
- [19] M. Ferer, C. Ji, G. S. Bromhal, J. Cook, G. Ahmadi, and D. H. Smith, Crossover from capillary to viscous fingering to immiscible unstable flow: Experiment and modelling, *Phys. Rev. E* **70**, 016303 (2004).
- [20] B. Sandnes, H. A. Knudsen, K. J. Måløy, and E. G. Flekkøy, Labyrinth patterns in confined granular-fluid systems, *Phys. Rev. Lett.* **99**, 038001 (2007).
- [21] H. A. Knudsen, B. Sandnes, E. G. Flekkøy, and K. J. Måløy, Granular labyrinth structures in confined geometries, *Phys. Rev. E* **77**, 021301 (2008).
- [22] B. Sandnes, E. G. Flekkøy, H. A. Knudsen, K. J. Måløy, and H. See, Patterns and flow in frictional fluid dynamics, *Nat. Commun.* **2**, 288 (2011).

- [23] D. Bensimon, L. P. Kadanoff, S. Liang, B. I. Shraiman, and C. Tang, *Rev. Mod. Phys.* **58**, 977 (1986).
- [24] C. Chevalier, A. Lindner, and E. Clément, *Phys. Rev. Lett.* **99**, 174501 (2007).
- [25] J. A. Eriksen, R. Toussaint, K. J. Måløy, E. G. Flekkøy, and B. Sandnes, Numerical approach to frictional fingers, *Phys. Rev. E* **92**, 032203 (2015).
- [26] J. A. Eriksen, R. Toussaint, K. J. Måløy, E. G. Flekkøy, O. Galland, and B. Sandnes, Pattern formation of frictional fingers in a gravitational potential, *Phys. Rev. Fluids* **3**, 013801 (2018).
- [27] C. Chevalier, A. Lindner, M. Leroux, and E. Clément, Morphodynamics during air injection into a confined granular suspension, *J. Non-Newtonian Fluid Mech.* **158**, 63 (2009).
- [28] J. M. Campbell, D. Ozturk, and B. Sandnes, Gas-driven fracturing of saturated granular media, *Phys. Rev. App.* **8**, 064029 (2017).
- [29] J. A. Eriksen, B. Marks, B. Sandnes, and R. Toussaint, Bubbles breaking the wall: Two-dimensional stress and stability analysis, *Phys. Rev. E* **91**, 052204 (2015).
- [30] H. A. Janssen, Versuche über getreidedruck in silozellen, *Z. Ver. Dtsch. Ing.* **39**, 1045 (1895).
- [31] T. S. Majmudar, and R. P. Behringer, Contact force measurements and stress-induced anisotropy in granular materials, *Nature* **435**, 23 (2005).
- [32] B. Marks, B. Sandnes, G. Dumazer, J. A. Eriksen, and K. J. Måløy, Compaction of granular material inside confined geometries, *Front. Phys.* **3**, 41 (2015).
- [33] E. Guazzelli, and O. Pouliquen, Rheology of dense granular suspensions, *J. Fluid Mech.* **852**, P1 (2018).
- [34] D. S. Springer, H. A. Loaiciga, S. J. Cullen, and L. G. Everett, Air permeability of porous materials under controlled laboratory conditions, *Ground Water* **36**, 558 (1998).
- [35] P. Macini, E. Mesini, and R. Viola, Laboratory measurements of non-Darcy flow coefficients in natural and artificial unconsolidated porous media, *J. of Pet. Sci. and Eng.* **77**, 365 (2011).
- [36] A.-K. Liedtke, F. Scheiff, F. Bornette, R. Philippe, D. W. Agar, and C. de Bellefon, Liquid-solid mass transfer for microchannel suspension catalysis in gas-liquid segmented flow, *Ind. Eng. Chem. Res.* **54**, 4699 (2015).
- [37] N. Eshtiaghi, F. Markis, S. D. Yap, J.-C. Baudez, and P. Slatter, Rheological characterisation of municipal sludge: A review, *Water Res.* **47**, 5493 (2013).
- [38] E. Hong, A. M. Yeneneh, T. K. Sen, H. M. Ang, and A. Kayaalp, A comprehensive review on rheological studies of sludge from various sections of municipal wastewater treatment plants for enhancement of process performance, *Adv. Coll. Int. Sci.* **257**, 19 (2018).